Contents lists available at ScienceDirect

Journal of Quantitative Spectroscopy and Radiative Transfer

journal homepage: www.elsevier.com/locate/jqsrt

Atomic structure, electron-impact excitation and collisional-radiative modelling for Ar II

N.E. McElroy [a],*, C.A. Ramsbottom [a], C.P. Ballance [a], N.R. Badnell [b], M.G. O'Mullane [b], S.D. Loch [c], E.N. Williamson [c]

[a] Astrophysics Research Centre, Queen's University Belfast, Belfast, BT7 1NN, Northern Ireland, United Kingdom
[b] Department of Physics, University of Strathclyde, Glasgow, G4 0NG, Scotland, United Kingdom
[c] Department of Physics, Auburn University, Auburn, 36832, AL, United States of America

ARTICLE INFO

ABSTRACT

The spectra from singly ionized argon Ar II has significant diagnostic capability in the characterization and modelling of both magnetically-confined fusion and astrophysical plasmas. The literature has several pre-existing data sets for Ar^+ but this paper presents the results from 3 new atomic structure and electron-impact scattering models in order to better constrain the differences in atomic data and how they impact well-known plasma diagnostics. Several independent atomic structure methodologies are employed to calculate the energy levels and transition probabilities for each model. The first approach employs a relativistic Dirac–Coulomb Hamiltonian model, the second approach uses a semi-relativistic Breit–Pauli Hamiltonian with the mass-velocity, Darwin and spin–orbit corrections, and in a third case an ICFT approach. Three atomic structure models provide a foundation for Dirac R-matrix, a semi-relativistic ICFT (Intermediate Coupling Frame Transformation) and a Breit–Pauli R-Matrix with Pseudostates (BPRMPS) calculation. Synthetic spectra utilizing these three data sets are compared against measurements taken at the Compact Toroidal Hybrid (CTH) stellarator, and the total radiative power loss is also benchmarked against previous calculations.

1. Introduction

The near-neutral ion stages of argon have many uses within the astrophysical and magnetically-confined fusion communities, from their fundamental properties quantifying the impact of magnetic fields in spectral broadening in B-Type Subdwarfs [1], the determination of density and temperature diagnostics ([2], to the moderation of plasma disruption by argon injection [3–5]). Many numerical plasma simulations are underpinned by the accuracy of the atomic structure and collisional calculations that form such models. The lack of comprehensive data sets for both radiative and all the collisional processes (excitation/ionization/recombination) for some elements with Z < Fe degrades the interpretation from these simulations. This paper shall focus on the atomic structure and collisional target of singly ionized Argon (Ar II) and the subsequent electron-impact excitation using both semi-relativistic and fully relativistic R-matrix methods.

From an astrophysical perspective Ar II lines in astrophysical plasmas were used in non-LTE modelling schemes to probe both B-type stars ([6–8] and B-type subdwarfs [1,9]), as well as extreme type helium stars [10]. Ar II was also recently observed in JWST spectra of the type 1a supernova SN2022pul [11] with the forbidden line among the

ground state fine-structure levels, $3s^2 3p^5 \, ^2P^o_{3/2}$ - $3s^2 3p^5 \, ^2P^o_{1/2}$ at 6.98 μm, dominating the spectrum. Additionally, singly ionized argon spectral lines have been used to constrain the elemental abundances of argon in planetary nebulae [12] and are employed within the XSTAR spectral modelling code [13].

From a magnetically-confined fusion perspective, argon has been employed in a wide variety of laboratory-based devices, i.e. DC magnetron [14], microwave driven plasmas [15], massive gas injections [16–18], argon shatter pellet injections [3–5] and as impurity seeding within scrape-off layer regions of fusion tokamaks [19,20]. The deliberate injection of impurities (Ne and Ar) into large scale tokamak devices such as ITER [21] and the proposed experimental reactor DEMO [22], mitigates plasma disruption and extends the lifetime of such devices. The main focus of the work here is to consider the modelling of Ar II at temperatures of 2–30 eV and at electron densities in the region of 1×10^{14} cm^{-3}.

Despite this widespread applicability of Ar II atomic data in the areas of laboratory, astrophysical and fusion plasmas, there remains a lack of availability of relevant data in current atomic databases such as OPEN-ADAS [23] and CHIANTI [24,25]. There has been some

---

work addressing the computation of energy levels, lifetimes and transition probabilities, however each of those publications have certain limitations. For example, the work of Hibbert [26] implemented a substantial and systematic configuration interaction approach to compute the transition rates for a small subset of 4p-4d transitions in Ar II. In addition, Afaneh et al. [27] performed relativistic configuration interaction calculations for a small selection of multipole transition rates and spectra for Ar II. A meaningful collisional radiative model requires a significantly more complete atomic dataset for parameters such as energy levels and A-values to ensure coverage of the wavelength range of interest. The situation relating to the availability of collisional atomic data for non-LTE modelling is similar. At the present time the only published fine-structure resolved electron impact excitation calculations have been undertaken by Dipti and Srivastava [28] and Kwon and Cho [29]. Both of these works utilize the fully relativistic distorted wave (DW) approximation to compute excitation cross sections and rate coefficients for transitions in Ar II. These DW calculations do not include coupling among the channels and do not include the Rydberg resonances that converge onto the target state thresholds in the low to intermediate energy regions. In these regions more sophisticated close-coupling methods such as the R-matrix method are generally required and to date only two calculations are listed in the literature [30,31]. Unfortunately both studies were performed in LS coupling only and hence no fine-structure resolved collision cross sections or excitation rates were computed.

The remainder of the paper is structured as follows. In Section 2 the atomic structure models used in the Ar II evaluations are discussed and the differing methods adopted are summarized. The radiative atomic data for the energy levels of the target states included as well as the A-values for transitions among these levels are compared and contrasted with known values. In Section 3 the results from the electron-impact excitation scattering calculations are presented. The cross sections and excitation rates for several important transitions are discussed in detail and an in depth comparison of models and methods adopted are outlined. In Section 4 the atomic data is included in a full non-LTE collisional radiative model. Level populations are investigated and some possible temperature and density diagnostic lines are identified. A synthetic spectra from the modelling is compared with the experimental observations from the Compact Toroidal Hybrid (CTH) tokamak in Auburn University and excellent agreement is found for several lines. Finally in Section 5 a summary is made and some conclusions drawn.

2. Atomic structure — methodology and models

The determination of quantities such as energy levels, radiative transition rates and level populations (not in LTE) requires a detailed description of the atomic system under consideration. In this paper, a series of Ar II models are generated using two separate structure packages, the fully relativistic code GRASP0 (General Relativistic Atomic Structure Package) and the semi-relativistic code AUTOSTRUCTURE. Below is a brief summary of the theory underpinning both methods.

The fully relativistic package GRASP0 published by Dyall et al. [32] is based upon the Multi-Configuration Dirac–Fock (MCDF) and the Multi-Configuration Breit–Pauli (MCBP) codes developed by Grant et al. [33] and McKenzie et al. [34]. The code solves the Time Independent Dirac Equation (TIDE),

$$H_D \phi = E\phi \tag{1}$$

where ϕ is the Dirac wavefunction, and E corresponds to the energy eigenvalues of the Dirac–Coulomb Hamiltonian which is defined (in atomic units) as weights proportional to $(2J + 1)$, as

$$H_D = \sum_{i=1}^{N} \left(c\boldsymbol{\alpha} \cdot \boldsymbol{p}_i + (\beta - \mathbf{I}_4)c^2 - \frac{Z}{r_i} \right) + \sum_{i>j=1}^{N} \frac{1}{r_{ij}}. \tag{2}$$

In Eq. (2) $\boldsymbol{\alpha}$ and β are related to the set of Pauli spin matrices, $\mathbf{I}_4$ is the 4×4 identity matrix, Z is the atomic number, c is the

speed of light, $\boldsymbol{p}$ is the momentum operator defined as $\boldsymbol{p} = -i\hbar\nabla$, r_i denotes the position of electron i and $r_{ij} = | r_i - r_j |$ is the interelectronic distance. Ultimately, GRASP0 determines an optimized set of atomic orbitals by variationally determining the minimum energy of this Hamiltonian making use of the extended average level (EAL) model within the code.

The AUTOSTRUCTURE package, is a major revision of its predecessor SUPERSTRUCTURE developed originally by Eissner [35] and substantially modified by Badnell [36] and Badnell [37]. Instead of the Dirac–Coulomb Hamiltonian, it adopts the semi-relativistic N-electron Breit–Pauli Hamiltonian given by

$$H_{BP} = H_{NR} + H_{RC} \tag{3}$$

where H_{NR} contains the non-relativistic operators

$$H_{NR} = \sum_{i=1}^{N} \left(-\frac{1}{2}\nabla_i^2 - \frac{Z}{r_i} \right) + \sum_{i>j=1}^{N} \frac{1}{r_{ij}} \tag{4}$$

and H_{RC} contains the first order relativistic correction operators:

$$H_{RC} = \frac{\alpha^2 Z}{2} \sum_{i=1}^{N} \frac{l_i \cdot s_i}{r_i^3} - \frac{\alpha^2}{8} \sum_{i=1}^{N} \nabla_i^4 - \frac{\alpha^2 Z}{8} \sum_{i=1}^{N} \nabla_i^2 \left(\frac{1}{r_i} \right) \tag{5}$$

The AUTOSTRUCTURE code generates a set of orbital parameters using a Thomas–Fermi–Dirac–Amaldi model potential for each nl. These potentials contain scaling parameters λ_{nl} for each nl orbital which are independently determined to minimize the difference from NIST [38] Energy values.

2.1. The models

The first Ar II model (Model 1) is a fully relativistic GRASP0 structure created from ten orbitals up to and including $n = 4$ (1s, 2s, 2p, 3s, 3p, 3d, 4s, 4p, 4d, 4f). A total of 31 non-relativistic configurations, listed in Table 1, were included in the wavefunction expansion giving rise to 1806 individual fine-structure levels. Configurations including single and double promotions from both the $3s$ and $3p$ orbitals were included to provide additional configuration interaction to improve the energy levels. The target state energies for the first 40 levels are presented in Table 5 under the heading Model 1 and compared with the available values from the NIST database [38].

Model 2 comprises of a AUTOSTRUCTURE Ar II model that includes fifteen orbitals up to $n = 5$, (1s, 2s, 2p, 3s, 3p, 3d, 4s, 4p, 4d, 5s, 5p, 5d, 5f, 5g). A total of 22 configurations were included in the representation of the target wavefunction and are listed in Table 2 in the first three columns alongside the λ_{nl} scaling parameters used for the bound orbitals in columns four and five. The level energies for the lowest 40 states are presented in Table 5 under the heading Model 2.

For the Ar II Model 3, AUTOSTRUCTURE is again employed but within a BP R-matrix with Pseudostates (RMPS) approximation [40,41]. The configurations given in Table 3 include associated Laguerre orbitals that were used to model the effect of high Rydberg and continuum states (up to $\bar{n} = 12, \bar{l} = 0 - 6$), which also improves the overall atomic structure. This Model 3 incorporated the 60 configurations listed in

Table 1
The configurations included in the wavefunction expansion for the GRASP0 Model 1.

Model 1 GRASP0			
$3s^2 3p^5$	$3s^2 3p^2 3d^3$	$3s3p^5 4p$	$3s3p^4 4d^2$	$3p^6 4f$
$3s^2 3p^4 3d$	$3s^2 3p^3 4s^2$	$3s3p^5 4d$	$3s3p^4 4f^2$	$3p^5 3d^2$
$3s^2 3p^4 4s$	$3s^2 3p^3 4d^2$	$3s3p^5 4f$	$3p^6 3d$	$3p^5 4s^2$
$3s^2 3p^4 4p$	$3s3p^6$	$3s3p^4 3d^2$	$3p^6 4s$	$3p^5 4p^2$
$3s^2 3p^4 4d$	$3s3p^5 3d$	$3s3p^4 4s^2$	$3p^6 4p$	$3p^5 4d^2$
$3s^2 3p^4 4f$	$3s3p^5 4s$	$3s3p^4 4p^2$	$3p^6 4d$	$3p^2 4f^2$
$3s^2 3p^3 3d^2$				

Table 2

The configurations included in the wavefunction expansion and the λ_{nl} scaling parameters for the AUTOSTRUCTURE Model 2.

Model 2 AUTOSTRUCTURE				
$3s^23p^5$	$3s^23p^45p$	$3s3p^54p$	$1s = 1.1000$	$4p = 1.0936$
$3s^23p^43d$	$3s^23p^45d$	$3s3p^54d$	$2s = 1.1000$	$4d = 1.1138$
$3s^23p^44s$	$3s^23p^45f$	$3s3p^54f$	$2p = 1.1000$	$4f = 1.1861$
$3s^23p^44p$	$3s^23p^45g$	$3s3p^55s$	$3s = 1.0967$	$5s = 1.1164$
$3s^23p^44d$	$3s3p^6$	$3s3p^55p$	$3p = 1.1076$	$5p = 1.0942$
$3s^23p^44f$	$3s3p^53d$	$3s3p^55d$	$3d = 1.1206$	$5d = 1.1166$
$3s^23p^45s$	$3s3p^54s$	$3s3p^55f$	$4s = 1.1159$	$5f = 1.1897$
		$3s3p^55g$		$5g = 1.1891$

Table 3

The configurations included in the wavefunction expansion for the AUTOSTRUCTURE Model 3.

Model 3 AUTOSTRUCTURE				
$3s^23p^5$	$3s^23p^46p$	$3s^23p^48s$	$3s^23p^49h$	$3s^23p^411f$
$3s^23p^43d$	$3s^23p^46d$	$3s^23p^48p$	$3s^23p^49i$	$3s^23p^411g$
$3s^23p^44s$	$3s^23p^46f$	$3s^23p^48d$	$3s^23p^410s$	$3s^23p^411h$
$3s^23p^44p$	$3s^23p^46g$	$3s^23p^48f$	$3s^23p^410p$	$3s^23p^411i$
$3s^23p^44d$	$3s^23p^46h$	$3s^23p^48g$	$3s^23p^410d$	$3s^23p^412s$
$3s^23p^44f$	$3s^23p^47s$	$3s^23p^48h$	$3s^23p^410f$	$3s^23p^412p$
$3s^23p^45s$	$3s^23p^47p$	$3s^23p^48i$	$3s^23p^410g$	$3s^23p^412d$
$3s^23p^45p$	$3s^23p^47d$	$3s^23p^49s$	$3s^23p^410h$	$3s^23p^412f$
$3s^23p^45d$	$3s^23p^47f$	$3s^23p^49p$	$3s^23p^410i$	$3s^23p^412g$
$3s^23p^45f$	$3s^23p^47g$	$3s^23p^49d$	$3s^23p^411s$	$3s^23p^412h$
$3s^23p^45g$	$3s^23p^47h$	$3s^23p^49f$	$3s^23p^411p$	$3s^23p^412i$
$3s^23p^46s$	$3s^23p^47i$	$3s^23p^49g$	$3s^23p^411d$	$3s3p^6$

Table 4

The λ_{nl} scaling parameters used in the AUTOSTRUCTURE Model 3. Note $5g+$ refers to the λ parameter used for all of the pseudostate orbitals.

Model 3 AUTOSTRUCTURE λ_{nl}					
$1s$	$=$	0.8195	$3d$	$=$	0.8202	$5s$	$=$	1.2000
$2s$	$=$	0.9406	$4s$	$=$	1.0674	$5p$	$=$	0.9422
$2p$	$=$	1.0640	$4p$	$=$	0.9600	$5d$	$=$	1.1892
$3s$	$=$	1.1223	$4d$	$=$	1.1611	$5f$	$=$	1.1992
$3p$	$=$	1.1000	$4f$	$=$	0.8755	$5g+$	$=$	-1.1575

Table 3. The corresponding λ_{nl} scaling parameters used on the bound orbitals are presented separately in Table 4 and the level energies for the first 40 levels are presented in Table 5. Adopting extensive Configuration Interaction (CI) expansions such as those described in Models 1, 2 and 3 does not necessarily ensure convergence in the corresponding representation of the target.

By employing different independent atomic structure codes with different relativistic/non-relativistic approximations we can assess the variation in the resulting energy levels and Einstein A-values as a quantifiable metric of the quality of the models in question, through validation against experimental measurements. Initially, we investigate the energy level separations of the target levels incorporated in the models and subsequently compute the transition rates or Einstein A-values for transitions among these levels. In each of these calculations care was taken to include the configurations listed in the NIST database [38], in the cases where we include only up to $n = 4$ (Model 1), the model includes all configurations up to $n = 4$ from NIST. The configuration set in each case was then expanded in order to converge towards a best structure for each model.

In Table 5 we present the configuration, term, levels and *ab initio* energy in Rydbergs relative to the $3s^23p^5\ ^2P^o_{3/2}$ ground state of Ar II, for the lowest 40 levels in all three Models 1, 2 and 3. Comparisons are made with the level energies available in NIST [39]. Comparing the calculated transition energies with their experimental counterparts, where available, provides an indication as to how each state involved

in the transition has been represented. From Table 5 we see that the relativistic GRASP0 Model 1 computes energy levels within approximately 3% for all 40 levels considered and particularly for the difficult $3s^23p^5\ ^2P^o_{1/2}$ fine-structure level of the ground state, this trend persists for all levels up to 90. The 22 configuration AUTOSTRUCTURE Model 2 indicates a similarly good agreement with many transition energies differing by less than 1%. The final and largest Model 3 which incorporates a pseudo-state expansion up to $n = 12$ produces energy levels which differ from NIST by less than 1% in the majority of states. In conclusion, all three models provide a wavefunction representation of the Ar II target suitable for inclusion in the subsequent electron-impact collisional analysis of interest in this paper.

The calculation of the transition rates (or A-values) requires that the energy separations, ΔE, are accurate to within a few percent. Deviations from this lead to inaccuracies scaled by $(\Delta E)^3$ for the dipole E1 and M1 transitions and $(\Delta E)^5$ for the quadrupole and $(\Delta E)^7$ for the octupole transitions. For electric dipole-allowed transitions, the A-value is given by

$$A_{i \to j} = \frac{\omega_{ji}^3}{3\pi c^3 \hbar \epsilon_0} \left| \langle \psi_j | \mathbf{D} | \psi_i \rangle \right|^2 \tag{6}$$

where ψ_i and ψ_j are the associated wavefunctions of the initial and final states, ω_{ij} is the angular frequency of the emitted photon, and $\mathbf{D}$ is the dipole operator. These A-values can be computed using the *ab initio* energies from Table 5 directly or alternatively by using the more spectroscopically accurate NIST values. In the latter case, as the A-value depends on the wavelength of the photon, which can be recovered using

$$\omega_{ji} = 2\pi \frac{c}{\lambda}, \tag{7}$$

the shifted A-value can be determined by

$$A_{ij}(\text{Shifted}) = \left(\frac{\lambda_{\text{Calculated}}}{\lambda_{\text{NIST}}} \right)^3 A_{ij}(\text{Unshifted}) \tag{8}$$

ensuring that the transition rates are computed using energies which have been shifted to the spectroscopically accurate NIST values.

We present in Table 6 the transition rates (in s^{-1}) for a selection of the strongest dipole allowed lines ($A_{ij} > 10^7\ \text{s}^{-1}$) among the lowest 40 levels in Ar II. The wavelength of the transition (in nm), the upper and lower index values of the levels set in Table 5, together with their configuration and LSJ level are listed in the first 7 columns of the table. Comparisons are made with the A-values available from NIST [42–47] alongside the accuracy rating allocated to the values in line with NIST standards. We can see that the highest NIST accuracy rating A has only been assigned to a few transitions whereas for transitions among the lowest lying levels 1–12 much lower accuracies of C-E are evident.

To investigate the extent to which neglecting a shift to spectroscopic energy levels would affect the collision strengths and effective collision strengths, we present in Table 6 the A-values determined from Models 1 and 3 with the energy levels shifted to the spectroscopically accurate NIST data and the A-values determined from Model 2 with *ab initio* energies.

For those transitions with a high grade A accuracy rating the agreement between all four sets of A-values is good. As the accuracy rating decreases so to does the agreement for some transitions, particularly those among the lowest lying levels from index 1 to 12. For the majority of these strong dipole lines, however, the conformity between all A-values is satisfactory.

All three models will now be incorporated into an electron-impact excitation collision calculation to compute the collision cross sections and excitation rates necessary for the modelling of astrophysical and fusion plasmas.

Table 5

The 40 lowest energy levels in Rydbergs for each Model 1, 2 and 3 compared to the values available in the NIST Database [39]. The listed percentage errors for each model are those computed relative to the NIST energies. For these levels, the mean absolute percentage errors for the three models are 1.15%, 0.99% and 0.69%, respectively.

Index	Config	Term	J	NIST (Ryd)	Model 1	% Err	Model 2	% Err	Model 3	% Err
1	$3s^23p^5$	$^2P°$	3/2	0.000000	0.000000	–	0.000000	–	0.000000	–
2	$3s^23p^5$	$^2P°$	1/2	0.013046	0.012622	−3.25	0.013605	4.29	0.013791	5.71
3	$3s3p^6$	^2S	1/2	0.990744	0.980918	−0.99	0.994930	0.42	0.994072	0.34
4	$3s^23p^43d$	^4D	7/2	1.205856	1.191989	−1.15	1.192028	−1.15	1.195135	−0.89
5	$3s^23p^43d$	^4D	5/2	1.207258	1.193431	−1.15	1.193368	−1.15	1.196520	−0.89
6	$3s^23p^43d$	^4D	3/2	1.20862	1.194750	−1.15	1.194662	−1.15	1.197863	−0.89
7	$3s^23p^43d$	^4D	1/2	1.209595	1.195670	−1.15	1.195591	−1.16	1.198825	−0.89
8	$3s^23p^44s$	^4P	5/2	1.223301	1.239993	1.36	1.205342	−1.47	1.211966	−0.93
9	$3s^23p^44s$	^4P	3/2	1.230994	1.247476	1.34	1.212832	−1.48	1.219564	−0.93
10	$3s^23p^44s$	^4P	1/2	1.235694	1.251867	1.31	1.217279	−1.49	1.224101	−0.94
11	$3s^23p^44s$	^2P	3/2	1.259769	1.287476	2.20	1.257229	−0.20	1.260185	0.03
12	$3s^23p^44s$	^2P	1/2	1.269015	1.294506	2.01	1.266087	−0.23	1.269197	0.01
13	$3s^23p^43d$	^4F	9/2	1.295697	1.295407	−0.02	1.282007	−1.06	1.286108	−0.74
14	$3s^23p^43d$	^4F	7/2	1.300534	1.299208	−0.10	1.286736	−1.06	1.290991	−0.73
15	$3s^23p^43d$	^4F	5/2	1.304093	1.302718	−0.11	1.290226	−1.06	1.294581	−0.73
16	$3s^23p^43d$	^4F	3/2	1.306497	1.305127	−0.10	1.292586	−1.06	1.297012	−0.73
17	$3s^23p^43d$	^2P	1/2	1.318694	1.329963	0.85	1.330705	0.91	1.335524	1.28
18	$3s^23p^43d$	^2P	3/2	1.327433	1.333901	0.49	1.341376	1.05	1.342499	1.13
19	$3s^23p^43d$	^4P	1/2	1.341641	1.334469	−0.53	1.335489	−0.46	1.343318	0.12
20	$3s^23p^43d$	^4P	3/2	1.344147	1.338792	−0.40	1.335835	−0.62	1.347395	0.24
21	$3s^23p^43d$	^4P	5/2	1.347545	1.338831	−0.65	1.341184	−0.47	1.349215	0.12
22	$3s^23p^44s$	^2D	3/2	1.354326	1.359685	0.40	1.356876	0.19	1.355824	0.11
23	$3s^23p^44s$	^2D	5/2	1.356352	1.362413	0.45	1.359510	0.23	1.358601	0.17
24	$3s^23p^43d$	^2F	7/2	1.359421	1.365305	0.43	1.361296	0.14	1.366477	0.52
25	$3s^23p^43d$	^2F	5/2	1.368247	1.371498	0.24	1.370591	0.17	1.376025	0.57
26	$3s^23p^43d$	^2D	3/2	1.371229	1.414391	3.15	1.384579	0.97	1.391911	1.51
27	$3s^23p^43d$	^2D	5/2	1.376809	1.417454	2.95	1.389053	0.89	1.396333	1.42
28	$3s^23p^43d$	^2G	9/2	1.405005	1.419958	1.06	1.412673	0.55	1.413547	0.61
29	$3s^23p^43d$	^2G	7/2	1.40521	1.420124	1.06	1.412573	0.52	1.413541	0.59
30	$3s^23p^44p$	$^4P°$	5/2	1.412857	1.420429	0.54	1.387012	−1.83	1.414665	0.13
31	$3s^23p^44p$	$^4P°$	3/2	1.415664	1.435223	1.38	1.389919	−1.82	1.417919	0.16
32	$3s^23p^44p$	$^4P°$	1/2	1.418917	1.435487	1.17	1.392835	−1.84	1.421054	0.15
33	$3s^23p^44p$	$^4D°$	7/2	1.432822	1.447954	1.06	1.416263	−1.16	1.434874	0.14
34	$3s^23p^44p$	$^4D°$	5/2	1.436826	1.452671	1.10	1.420747	−1.12	1.439970	0.22
35	$3s^23p^44p$	$^4D°$	3/2	1.441331	1.456773	1.07	1.424592	−1.16	1.444074	0.19
36	$3s^23p^44p$	$^4D°$	1/2	1.443703	1.459051	1.06	1.426734	−1.18	1.446338	0.18
37	$3s^23p^44p$	$^2D°$	5/2	1.446457	1.466478	1.38	1.434771	−0.81	1.452489	0.42
38	$3s^23p^44p$	$^2D°$	3/2	1.452499	1.473951	1.48	1.441697	−0.74	1.458932	0.44
39	$3s^23p^44p$	$^2P°$	1/2	1.455353	1.487876	2.23	1.446262	−0.62	1.463146	0.54
40	$3s^23p^44p$	$^2P°$	3/2	1.460209	1.492293	2.20	1.451684	−0.58	1.467748	0.52

3. Electron-impact excitation — calculation of collisional data

3.1. Methodology

The *R*-matrix method is accepted as one of the most accurate and powerful methods used to compute collision cross sections for electron-impact excitation. The theory is only summarized here, but the reader is directed to the publication of Burke [48] for a full description of the theory. Central to the *R*-matrix framework is the partitioning of the configuration space describing the physical system of the *N*-electron target and scattered electron into two regions, the internal and external regions.

In the inner region, the full many-bodied Hamiltonian is addressed as opposed to the external region where the scattered electron moves in a multipole expansion created by the target. A radius *a*, centred at the nucleus is chosen so as to encapsulate the atomic charge distribution of the target states of interest as dictated by the most diffuse orbital of the target. This boundary acts as an interface between the two regions. The *R*-matrix is defined as follows,

$$R_{ij} = \frac{1}{2a} \sum_{k}^{N+1} \frac{\omega_{ik}(a)\omega_{jk}(a)}{E_k^{N+1} - E}, \qquad (9)$$

where E_k^{N+1} are the eigenenergies of the $(N + 1)$ Hamiltonian, E is the energy of the incident electron, and ω_{ik} are the energy independent surface amplitudes.

In the internal region, where $r \leq a$, the scattered electron interacts strongly with the target and the resulting intermediate electron-target complex very much resembles a bound state. Consequently, exchange and correlation effects between the scattered electron and the target electrons are strong.

In the external region, where $r \geq a$, the scattered electron is considered to be free from the charge distribution of the target and the electron now moves only in the long-range multipole potential of the target. The interaction between the two bodies is therefore weak and hence exchange and correlation effects can be neglected, thereby simplifying the calculation considerably.

The scattering observables of interest in this publication are the electron-impact excitation collision strengths and Maxwellian averaged effective collision strengths. Both can be determined from the total scattering cross sections $\sigma_{i \to j}$ for a transition from an initial atomic or ionic target state i to a final atomic or ionic target state j following the collision. The collision strengths are related to the cross section $\sigma_{i \to j}$ by the relation,

$$\Omega_{i \to j} = \frac{g_i k_i^2}{\pi a_0^2} \sigma_{i \to j}, \qquad (10)$$

where g_i is the statistical weight of the initial state, k_i^2 is the energy of the incident electron in Rydbergs, and a_0 is the Bohr radius. The collision strengths $\Omega_{i \to j}$ are dimensionless symmetric quantities which will be finite at threshold for positively charged ions. Complex structure manifests as a series of resonances converging onto the target state thresholds and is generally confined to the low energy region below the ionization threshold. Beyond this threshold, as E becomes infinitely large, the collision strength will tend towards a high energy limit determined by the type of transition involved.

Table 6

Einstein A-Values (in s^{-1}) for a selection of strong electric dipole allowed transitions in Ar II. NIST – values obtained from the NIST database [42–47], Model 1 (corrected), Model 2 (uncorrected), Model 3 (corrected) – values obtained from Models 1,2 and 3 with either the energy levels shifted to the spectroscopically accurate NIST values or uncorrected and the *ab initio* energies used.

Wavelength (nm)	j	i	Upper level j		Lower level i		NIST	Acc	Model 1 (shifted)	Model 2 (unshifted)	Model 3 (shifted)
91.98	3	1	$3s3p^6$	$^2S_{1/2}$	$3s^23p^5$	$2P^o_{3/2}$	1.40E+08	C	1.14E+08	2.00E+07	1.32E+08
93.21	3	2	$3s3p^6$	$^2S_{1/2}$	$3s^23p^5$	$2P^o_{1/2}$	6.70E+07	C	5.63E+07	1.05E+07	6.63E+07
74.03	9	1	$3s^23p^44s$	$^4P_{3/2}$	$3s^23p^5$	$2P^o_{3/2}$	3.10E+07	E	3.19E+07	1.92E+07	1.89E+07
72.34	11	1	$3s^23p^44s$	$^4P_{3/2}$	$3s^23p^5$	$2P^o_{3/2}$	2.30E+09	D	4.11E+09	2.94E+09	2.33E+09
73.09	11	2	$3s^23p^44s$	$^4P_{3/2}$	$3s^23p^5$	$2P^o_{1/2}$	4.50E+08	D	6.84E+08	4.90E+08	3.87E+08
71.81	12	1	$3s^23p^44s$	$^4P_{1/2}$	$3s^23p^5$	$2P^o_{3/2}$	9.50E+08	D	1.70E+09	1.22E+09	9.76E+08
72.56	12	2	$3s^23p^44s$	$^4P_{1/2}$	$3s^23p^5$	$2P^o_{1/2}$	1.90E+09	D	2.97E+09	2.22E+09	1.76E+09
440.10	30	4	$3s^23p^44p$	$^4P^o_{5/2}$	$3s^23p^43d$	$4D_{7/2}$	3.04E+07	B	5.05E+07	3.43E+07	2.87E+07
443.10	30	5	$3s^23p^44p$	$^4P^o_{5/2}$	$3s^23p^43d$	$4D_{5/2}$	1.09E+07	B	1.54E+07	1.24E+07	1.12E+07
480.60	30	8	$3s^23p^44p$	$^4P^o_{5/2}$	$3s^23p^44s$	$4P_{5/2}$	7.80E+07	A	7.98E+07	7.16E+07	9.02E+07
500.93	30	9	$3s^23p^44p$	$^4P^o_{5/2}$	$3s^23p^44s$	$4P_{3/2}$	1.51E+07	B	2.02E+07	1.68E+07	1.89E+07
437.13	31	5	$3s^23p^44p$	$^4P^o_{3/2}$	$3s^23p^43d$	$4D_{5/2}$	2.21E+07	B	3.76E+07	2.34E+07	1.90E+07
440.01	31	6	$3s^23p^44p$	$^4P^o_{3/2}$	$3s^23p^43d$	$4D_{3/2}$	1.60E+07	B	2.39E+07	1.70E+07	1.49E+07
473.59	31	8	$3s^23p^44p$	$^4P^o_{3/2}$	$3s^23p^44s$	$4P_{5/2}$	5.80E+07	A	5.77E+07	5.54E+07	6.76E+07
493.32	31	9	$3s^23p^44p$	$^4P^o_{3/2}$	$3s^23p^44s$	$4P_{3/2}$	1.44E+07	A	1.43E+07	1.68E+07	1.65E+07
506.20	31	10	$3s^23p^44p$	$^4P^o_{3/2}$	$3s^23p^44s$	$4P_{1/2}$	2.23E+07	B	2.93E+07	2.43E+07	2.80E+07
433.20	32	6	$3s^23p^44p$	$^4P^o_{1/2}$	$3s^23p^43d$	$4D_{3/2}$	1.92E+07	B+	3.04E+07	1.93E+07	1.56E+07
435.22	32	7	$3s^23p^44p$	$^4P^o_{1/2}$	$3s^23p^43d$	$4D_{1/2}$	2.12E+07	B	3.49E+07	2.37E+07	2.03E+07
484.78	32	9	$3s^23p^44p$	$^4P^o_{1/2}$	$3s^23p^44s$	$4P_{3/2}$	8.49E+07	B	8.94E+07	8.09E+07	1.00E+08
401.39	33	4	$3s^23p^44p$	$^4D^o_{7/2}$	$3s^23p^43d$	$4D_{7/2}$	1.05E+07	A	1.66E+07	1.25E+07	9.45E+06
434.81	33	8	$3s^23p^44p$	$^4D^o_{7/2}$	$3s^23p^44s$	$4P_{5/2}$	1.17E+08	A	1.20E+08	1.37E+08	1.31E+08
664.37	33	13	$3s^23p^44p$	$^4D^o_{7/2}$	$3s^23p^43d$	$4F_{9/2}$	1.47E+07	B	2.71E+07	1.85E+07	1.55E+07
426.65	34	8	$3s^23p^44p$	$^4D^o_{5/2}$	$3s^23p^44s$	$4P_{5/2}$	1.64E+07	B	2.42E+07	2.67E+07	2.21E+07
442.60	34	9	$3s^23p^44p$	$^4D^o_{5/2}$	$3s^23p^44s$	$4P_{3/2}$	8.17E+07	A	8.61E+07	1.01E+08	9.87E+07
514.53	34	11	$3s^23p^44p$	$^4D^o_{5/2}$	$3s^23p^44s$	$2P_{3/2}$	1.06E+07	B	2.84E+06	2.88E+06	4.00E+06
668.43	34	14	$3s^23p^44p$	$^4D^o_{5/2}$	$3s^23p^43d$	$4F_{7/2}$	1.07E+07	B+	2.31E+07	1.61E+07	1.32E+07
487.99	37	11	$3s^23p^44p$	$^2D^o_{5/2}$	$3s^23p^44s$	$2P_{3/2}$	8.23E+07	A	7.88E+07	8.41E+07	9.90E+07

In many astrophysical and laboratory plasmas the free electron distribution approximates a Maxwellian distribution and hence the excitation rates of interest can be expressed in terms of a thermally averaged effective collision strength. These effective collision strengths, (Y_{ij}), are obtained by averaging the finely resolved collision strengths over a Maxwellian distribution of electron velocities so that,

$$Y_{ij}(T_e) = \int_0^\infty \Omega_{i \to j} e^{-\epsilon_j/kT_e} d\left(\frac{\epsilon_j}{kT_e}\right), \qquad (11)$$

where ϵ_j defines the remaining kinetic energy of the incident electron following excitation, T_e is the electron temperature (in Kelvin), and k is Boltzmann's constant. It is these Maxwellian averaged effective collision strengths that are commonly used by astrophysical and plasma modellers in their diagnostic applications due their slow variation as a function of temperature.

It is important to note that convergence of the summation over the partial collision strengths to determine the total collision strength, $\Omega_{i \to j}$, for the optically allowed transitions is significantly slower than that for the forbidden lines. Hence, to ensure convergence, a large number of partial wave collision strength contributions are required for these transitions which can be computationally intensive. To rectify this a 'top-up' procedure is employed to estimate the contributions from partial waves with high angular momenta, as described by Burgess and Sheorey [49] and Burke and Seaton [50].

Similarly, while collision strengths for forbidden transitions fall-off as $1/\epsilon^2$, spin allowed non-dipole transitions tend to a constant (given by the infinite energy Born limit) while dipole-allowed diverge logarithmically in energy and are given by the Bethe limit of $\frac{4}{3}S \ln(\epsilon)$ in terms of the radiative line strength (S) for the transition [51]. These limits are used to aid evaluation of the convolution integral (11) given that the *R*-matrix method is more computationally demanding at high energies.

3.2. The R-matrix electron-impact excitation calculations

There are several variants of the *R*-matrix computer codes currently available and three presented here ((P)DARC, ICFT and BP RMPS) that are utilized in the present calculations to compute the collision strengths and effective collision strengths for the electron-impact excitation of Ar II. The three scattering calculations correspond to each of the three atomic structure models described in the previous section.

To summarize, the first model employs a 31 non-relativistic configuration GRASP0 Model 1 atomic structure into the fully relativistic Parallel Dirac Atomic R-matrix Code PDARC [52] based upon the serial versions of the code developed by Norrington [53], and Norrington and Grant [54]. We label this calculation Coll1-DARC. This suite of *R*-matrix packages permits fully relativistic jj coupled scattering calculations to be performed by solving the Dirac equation with the Dirac Hamiltonian. The 31 configurations included gave rise to 1806 individual fine-structure levels but only the lowest lying 250 were retained in the close-coupling expansion of the total wavefunction to reduce the computational effort required. Of these 250 levels the first 91 were shifted to their spectroscopic positions observed by NIST and the remaining 159 energy levels remained unshifted. This ensured that, where possible, the threshold positions were at their correct values aiding the identification of lines for spectral analysis. A total of 25 continuum orbitals were included for each channel angular momentum and the R-matrix boundary radius at which a zero logarithmic derivative is imposed on the expansion was set at 24.22 a.u. These parameters were sufficient to cover the range of electron-impact energies considered, 0 - 8 Ryds. A very fine mesh of incident electron energies (10^{-4} Ryds) guaranteed the delineation of the resonance structures converging onto the target state thresholds. The R-matrix calculations were carried out for all partial waves with total angular momentum J ≤ 40, for both odd and even parities and doublet and quartet spin states. For the optically forbidden transitions this is sufficient to ensure that the corresponding collision strengths have converged. However, for the allowed transitions it is necessary to include higher partial waves J > 40. To estimate the contribution to the

collision strength of such allowed transitions from $J > 40$, we use the Bethe sum-rule of Burgess and Sheorey [49] for the dipole transitions and for quadrupole and higher it is assumed that the partial collision strengths form a geometric series as a function of partial wave. Finally the high energy Bethe and Born limits were computed to check the validity of the collision strengths at higher energies.

The second collision calculation incorporates the 15 orbital, 22 configuration AUTOSTRUCTURE Model 2 into the intermediate coupling frame transformation (ICFT) *R*-matrix suite of programmes. We label this calculation Coll2-ICFT. The benefit of the ICFT method is that the inner region calculation is effectively in LS coupling with the inclusion of the mass-velocity and Darwin terms. This reduces the size of the matrix diagonalisations in the inner region, with level-level collisions achieved by a transformation of K-matrices in the outer region. However, with the widely available computational resources of massively parallel cluster supercomputers, the wall-time requirement for diagonalization of large matrices is becoming an increasingly moot point.

For non-pseudostate calculations, the ICFT method is equivalent to a Breit–Pauli *R*-matrix (BPRM) method neglecting the spin–orbit splitting of terms in the inner region. In essence, ICFT initially performs an LS-coupled close coupling calculation for the target in the inner region including only the mass-velocity and Darwin one-body relativistic operators. The LS-coupled K reactance matrices are then recoupled to jK-coupling and finally transformed to jj intermediate coupling using the Breit–Pauli term coupling coefficients.

The relevant *R*-matrix codes for the ICFT collision calculations are the inner region codes of Hummer et al. [55] and Berrington et al. [56], the outer regions STGF programme of Berrington et al. [57] and Badnell [58], alongside the ICFT frame transformation code of Griffin et al. [59]. This calculation included the lowest lying 426 target levels in the expansion of the total wavefunction, significantly larger than Coll1-DARC. In an attempt to investigate the consequence of shifting the target state energies to their exact positions determined in NIST and ensure no significant divergence between shifted and unshifted collisional calculations is found, in this scattering calculation the 426 levels remain unshifted and are positioned at their *ab initio* values computed in AUTOSTRUCTURE. A full exchange calculation was performed for partial waves with angular momentum $J = 0\text{-}12$, augmented by a non-exchange evaluation for partial waves $J = 13\text{-}30$. Finally the top-up procedure was added for partial waves $J \rightarrow \infty$. A total of 40 continuum basis orbitals ensured coverage of incident electron energies up to approximately 7 Ryds and a fine energy mesh (10^{-3} Ryds) resulted in a proper resolution of the Rydberg resonances converging onto the target state thresholds. Again the high energy Bethe and Born limits were computed to test the behaviour of the collision strengths at high energies.

The third and final electron-impact excitation calculation performed an extensive 60 configuration AUTOSTRUCTURE Model 3 into the Breit–Pauli *R*-matrix with Pseudostates suite of codes. We label this calculation Coll3-BP. In this semi-relativistic method the close-coupling expansion of the target wavefunction is constructed in intermediate coupling where the spin–orbit operator is included in the (N + 1)-electron Hamiltonian. The 60 configurations resulted in a 1444 fine-structure level model, 250 levels arising from 110 terms were retained in the close-coupling expansion. Similar to Coll1-DARC, the first 91 levels were shifted to their NIST positions and the remaining 159 were left unshifted due to a lack of available data. The *R*-matrix boundary radius was set at 51.64 a.u. covering a range of incident electron energies up to 4.5 Ryd. Finally, 32 continuum orbitals were included for each orbital angular momentum, and all partial waves with $J \leq 40$ were included with a fine energy mesh of 1×10^{-4} Ryd for partial waves $J \leq 12$ and a coarser energy mesh of 2×10^{-3} for $J > 12$. Again the top-up procedure was adopted for partial waves above $J > 40$ and the high energy Bethe and Born limits were computed [49]. With RMPS

calculations, it is often the most diffuse pseudo-orbital that sets the size of the R-matrix radius.

In the next section we compare the results obtained from these three electron-impact excitation calculations for a number of allowed and forbidden transitions. By comparing the collision strengths and effective collision strengths that emerge from these three different models using three different *R*-matrix methods, we can test the convergence of the atomic data computed.

3.3. Results section — collision strengths and effective collision strengths

In Fig. 1 we present the collision strength (left panel) as a function of incident electron energy (Ryds) and the corresponding Maxwellian averaged effective collision strength (right panel) as a function of electron temperature (K) for the transition among the ground state doublet fine-structure split levels, $3s^23p^5\ ^2P^o_{3/2}$ - $3s^23p^5\ ^2P^o_{1/2}$ (1–2). As stated earlier, this forbidden line was recently observed in JWST spectra of the type 1a supernova SN2022pul and was found to dominate the spectra at 6.98 μm. A comparison of the collision strengths from the three calculations for this weak transition is important given its likelihood to have a significant population at low temperatures due to the small energy separation in the transition. Coll1-DARC and Coll2-ICFT both produce an exponential drop in collision strength above threshold compared to a more gradual decline for Coll3-BP for similar electron energies, the high mesh resolution ensures that this is a real difference between the three models.

The positioning and magnitudes of the Rydberg resonances converging onto the target state thresholds agree well between 0.75–1.25 Ryds and the disparity between the background cross section is satisfactory. The corresponding effective collision strengths agree well for all temperatures considered with the best agreement occurring between the Coll1-DARC and Coll2-ICFT calculations, the Coll3-BP results lie consistently above these two but exhibits a similar behaviour.

The first E1 dipole resonance line in Ar II is relatively weak and involves the transition between the ground state and the $3s3p^6\ ^2S_{1/2}$ doublet state at 0.9907 Ryds. The three collision strengths computed in Coll1-DARC, Coll2-ICFT and Coll3-BP are presented in Fig. 2 and show excellent agreement across the Rydberg resonance region, with one main exception. A strong resonance feature appears just above threshold in the Coll1-DARC collision strength that significantly enhances the corresponding Maxwellian averaged effective collision strength for very low temperatures. In this temperature region the largest differences occur between the three calculations. As the temperature increases, however, the three sets of data agree reasonably well particularly between the Coll1-DARC and Coll3-BP datasets where the high temperature rates tend towards a similar high energy Bethe limit. The effective collision strength from the Coll2-ICFT calculation tends towards a lower limit for this allowed line, as indicated by the comparison of the Einstein A-values in Table 6.

Figs. 1 and 2 compare and contrast two weak transitions, one forbidden (1–2) and one allowed (1–3) and the overall agreement found between the three collision calculations gives some assurance as to the reliability of the atomic data provided. It is also prudent to assess the accuracy of some of the strongest degenerate dipole transitions as these transitions can be effective diagnostic tools for plasma modelling. In Figs. 3 and 4 we present the collision strengths and effective collision strengths for two significantly stronger E1 lines, the $3s^23p^4(^3P)4s\ ^4P_{5/2}$ - $3s^23p^4(^3P)4p\ ^4P^o_{5/2}$ (8–30) and the $3s^23p^4(^3P)4s\ ^2P_{3/2}$ - $3s^23p^4(^3P)4p\ ^2D^o_{5/2}$ (11–37). These two lines are more than ten times stronger than the previous two and have significant application in both fusion and astrophysical plasma modelling via their widespread usage as the 480.60/487.99 nm diagnostic line ratio. Clearly evident is the excellent agreement, for both transitions, between all three sets of data across the full incident energy and temperature ranges of interest. The main difference arises in the background cross section which is sensitive to the A-value of the transition computed in each model. This
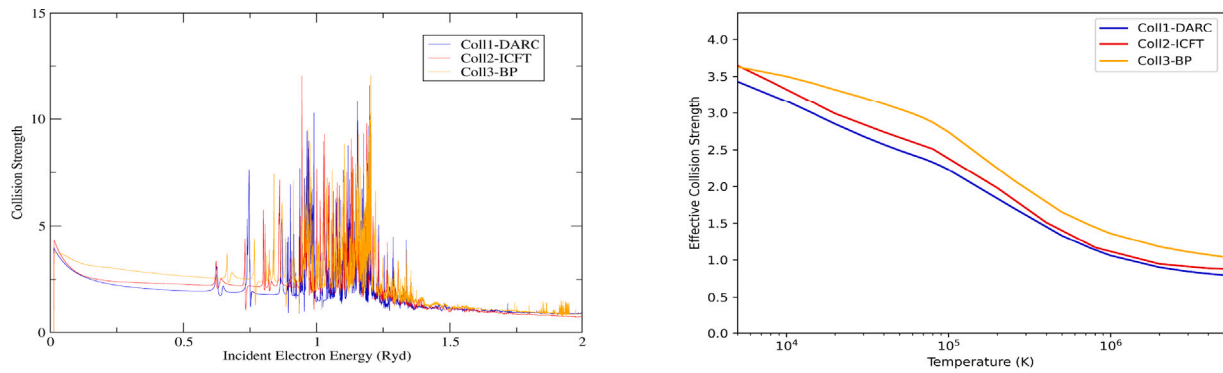
Fig. 1. Collision Strength as a function of incident electron energy in Ryds (left panel) and corresponding effective collision strength as a function of electron temperature in K (right panel) for the $3s^23p^5$ $^2P^o_{3/2}$ - $3s^23p^5$ $^2P^o_{1/2}$ (1–2) transition in Ar II. The solid blue, red and yellow curves represent the three calculations Coll1-DARC, Coll2-ICFT and Coll3-BP respectively.
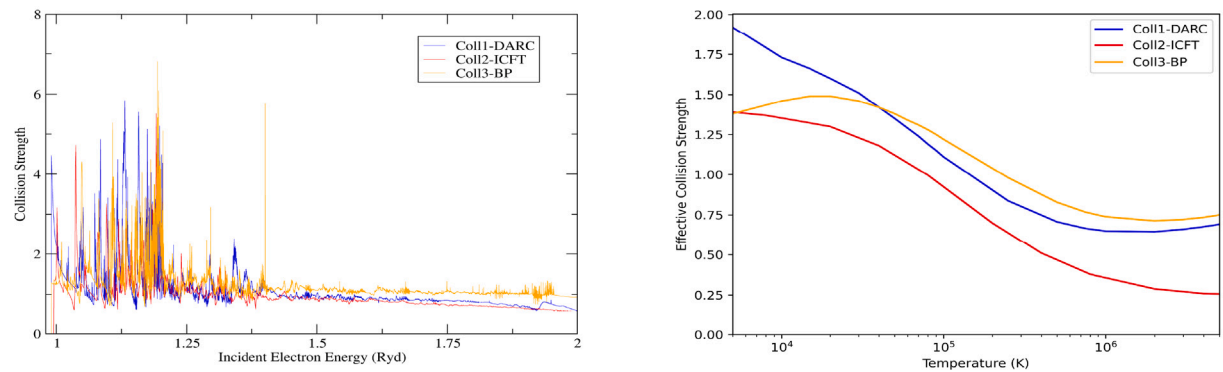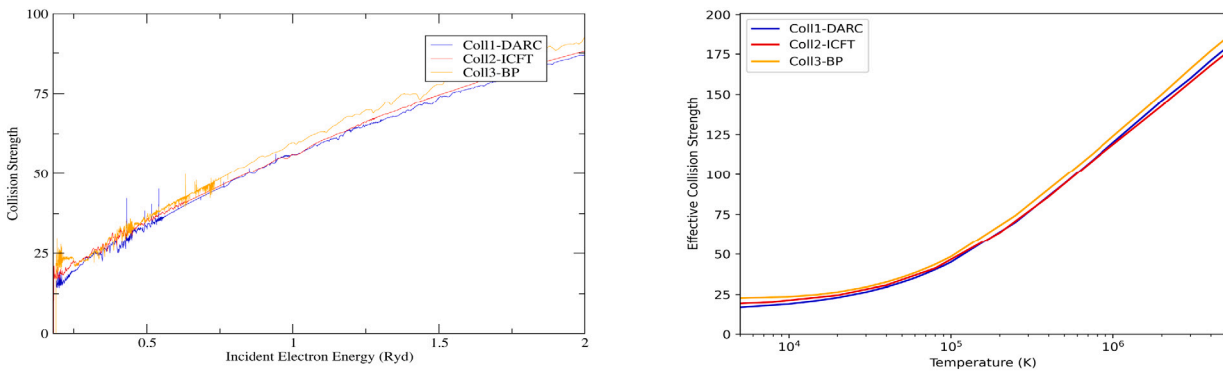

Fig. 2. Collision Strength as a function of incident electron energy in Ryds (left panel) and corresponding effective collision strength as a function of electron temperature in K (right panel) for the $3s^23p^5$ $^2P^o_{3/2}$ - $3s3p^6$ $^2S_{1/2}$ (1–3) transition in Ar II. The solid blue, red and yellow curves represent the three calculations Coll1-DARC, Coll2-ICFT and Coll3-BP respectively.

Fig. 3. Collision Strength as a function of incident electron energy in Ryds (left panel) and corresponding effective collision strength as a function of electron temperature in K (right panel) for the $3s^23p^4(^3P)4s$ $^4P_{5/2}$ - $3s^23p^4(^3P)4p$ $^4P^o_{5/2}$ (8–30) transition in Ar II. The solid blue, red and yellow curves represent the three calculations Coll1-DARC, Coll2-ICFT and Coll3-BP respectively.

lack of disparity would suggest that the variety of models included in the scattering calculations and the different methodologies of the approaches used have produced datasets that exhibit excellent convergence. Additional differences such as the number of levels included (250 for Coll1-DARC and Coll3-BP and 426 for Coll2-ICFT), the shifting of the target thresholds to their observed positions (Coll1-DARC and Coll3-BP), the number of continuum terms, the total number of partial waves included as well as the energy mesh adopted in the resonance region, do not appear to have significantly affected the final results. Additionally, the agreement of the three calculations extends well into the higher temperature region with the main separation arising from slightly different infinite energy points at that regime. In the next

section we further test this assumption of accuracy by performing some non-LTE collisional radiative modelling.

4. Collisional-radiative modelling

In this section we adopt the Generalised Collisional Radiative (GCR) theory of Summers et al. [60] as implemented in a Python code (ColRadPy) [61]. The minimal input required to investigate the plasma characteristics of Ar II are the energy levels, A-values, relevant quantum numbers and effective collision strengths as described in the previous section. While the calculated data can be employed for a wide range of temperature and plasma densities, in this paper we limit our modelling
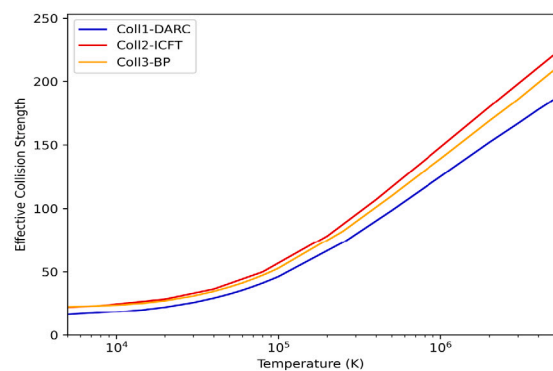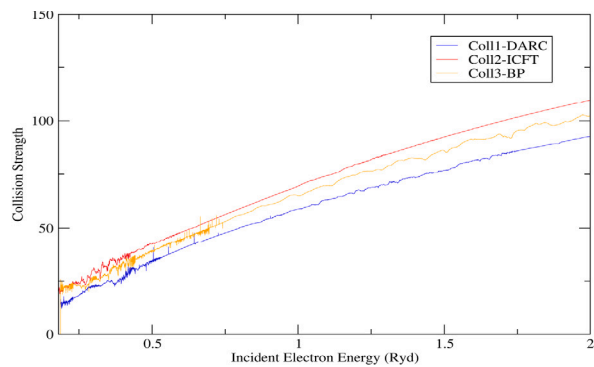
Fig. 4. Collision Strength as a function of incident electron energy in Ryds (left panel) and corresponding effective collision strength as a function of electron temperature in K (right panel) for the $3s^2 3p^4 (^3P) 4s\ ^2P_{3/2}$ - $3s^2 3p^4 (^3P) 4p\ ^2D^o_{5/2}$ (11–37) transition in Ar II. The solid blue, red and yellow curves represent the three calculations Coll1-DARC, Coll2-ICFT and Coll3-BP respectively.
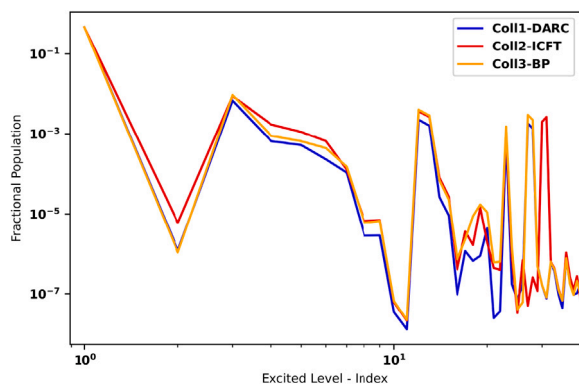
Fig. 5. Calculated fractional populations in a quasi-static collisional radiative calculation for the first 40 Excited states for each collisional calculation, at $T_e = 7\,eV$ and $n_e = 10^{11}\ cm^{-3}$, with first excited state at index 1.

to the temperature range $2 \leq T_e \leq 30$ eV and plasma densities between $1 \times 10^9 \leq n_e \leq 1 \times 10^{14}\ cm^{-3}$, as these represent the range of values of relevance for the coronal to collisional radiative regimes. As we employ three different datasets this should enable us to ensure confidence in the atomic data and ultimately in our interpretation of the plasma diagnostics.

4.1. Population modelling

Initially, we verify whether the underlying atomic structures and collisional results vary significantly between the three models. All models have been shown to reproduce the atomic structure of Ar II to a suitably high degree of accuracy, and hence, it is expected that the resulting populations should be similar if the collisional data is also. This assertion is tested in Fig. 5 where the fractional populations are given as a function of level index for the first 40 levels. The temperature was chosen to be 7 eV and the density chosen to be $10^{11} cm^{-3}$ in the modelling as this was within the operating parameters of the Compact Toroidal Hybrid (CTH) at Auburn University [62]. The plot is limited to the first 40 excited levels.

The largest disagreement between the three calculations arises when the level index between Coll2-ICFT is mismatched with the other two calculations due to there being no shift to experimental energy levels. The fractional populations match very well for the vast majority of levels suggesting a good basis for the collisional radiative modelling.

A secondary check was undertaken to assess each collisional calculation's suitability for collisional-radiative modelling by investigating the line radiation power loss coefficient (PLT) which gives an indication of the overall radiative power loss within the plasma emission. In Fig. 6

the total PLT coefficient is plotted as a function of temperature (in eV) for each of the three calculations discussed in the present work as well as the earlier computations of Summers [23] and Griffin et al. [30] for completeness. The large disagreement between the two previous works provided one of the major motivations for the new calculations presented in this paper. To ensure that we are comparing calculations consistently, the left hand panel of Fig. 6 compares the PLT curves computed when only the $n = 4$ levels that lie below the ionization potential were retained (Coll1-DARC retained 109 levels, Coll2-ICFT 113 levels and Coll3-BP 114 levels). The agreement between the three plots is excellent across the full temperature range considered. The right hand panel of Fig. 6 displays the PLT curves predicted when all levels, including any $n = 5$ levels below the ionization potential, were included in the computations (Coll1-DARC 109 levels, Coll2-ICFT 222 levels and Coll3-BP 250). As expected the Coll2-ICFT and Coll3-BP curves deviate from the Coll1-DARC results due to the effect of including the $n = 5$ levels in the PLT calculations. Clearly, these additional levels enhance the PLT. Finally, to investigate convergence it is important to check whether the addition of the $n = 6$ levels further enhances the PLT but these are computationally large R−matrix calculations. Instead two non-resonant distorted wave IC evaluations were performed which allow us to test the convergence of the PLT values. It should be noted, however, that DW calculations are well known to overestimate the collision cross sections for low charge states, see for example [63] for Hydrogen ionization. In the right hand panel of Fig. 6 it is found that the difference in PLT when going from $n = 5$ to $n = 6$ is negligible to the convergence of the PLT. Hence we can conclude that the PLT curves from either the Coll2-ICFT and Coll3-BP represent the most accurate available and the conformity between the two gives credence to the results presented.

4.2. Temperature and density dependence analysis of possible diagnostic lines and line-ratios

The excitation Photon Emissivity Coefficient (PEC) is a derived coefficient for predicting individual spectrum line emission and is defined as

$$PEC^{exc}_{j \to i} = A_{ji} F^{exc}_j \qquad (12)$$

where F^{exc}_j is the effective contributions to the population of the upper excited level j of the transition from excitation from the ground as in this modelling it was the only designated metastable and A_{ji} is the Einstein A-value for the transition from j to i. Figs. 7 and 8 represent a selection of line sensitivities for two strong dipole transitions (8–33 and 11–37). Both record a lack of density dependence in a low-density regime between $10^9 \leq n_e \leq 10^{11}\ cm^{-3}$ and a marked variance in the orders of magnitude in the excitation photon emissivity coefficient (PEC) across the temperature regime between 4 and 10 eV. In the
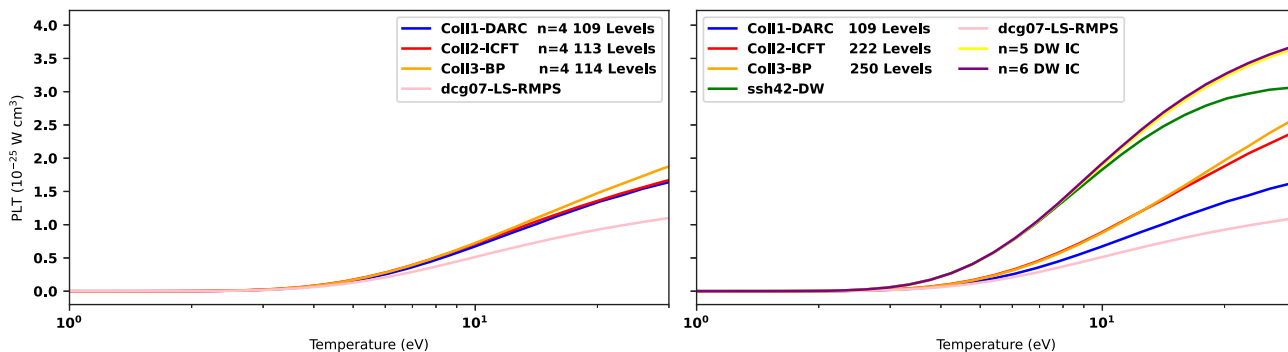
Fig. 6. Calculated Power Loss PLT for the three calculations between 0 and 20eV is shown on the left. The ssh42-DW PLT is as recovered from Summers [23] for the ssh42_cs_ic#ar1.dat adf04 file of Stuart Henderson at UKAEA, whilst dcg07-LS-RMPS refers to Griffin et al. [30]. The $n = 5$ and $n = 6$ DW IC are non-resonant distorted wave calculations undertaken by the authors. All adf04 files had autoionizing levels removed prior to calculation of PLT. On the left Coll2-ICFT and Coll3-BP are reduced to only $n = 4$ states and compared with the $n = 4$ adf04 files of Coll1-DARC and dcg07-LS-RMPS. This figure was prepared using results from ADAS208. Summers [23].
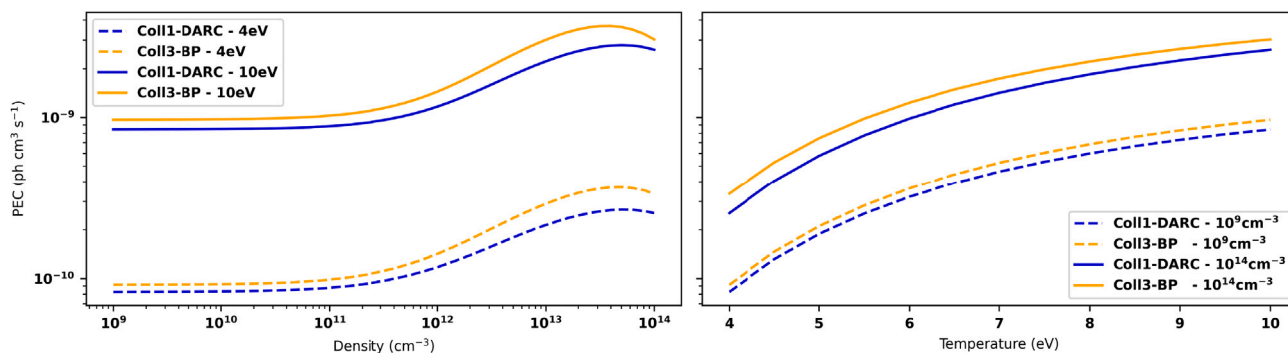
Fig. 7. Photon emissivity coefficient (PEC) as a function of density (left panel) and temperature (right panel) for the $3s^2 3p^4(^3P)4s\ ^4P_{5/2}$ - $3s^2 3p^4(^3P)4p\ ^4D^o_{7/2}$ $(8-33)$ transition. The blue and orange lines denote the Coll1-DARC and Coll3-BP calculations respectively, with dashed lines representing low densities and temperatures and the solid lines representing high densities and temperatures.
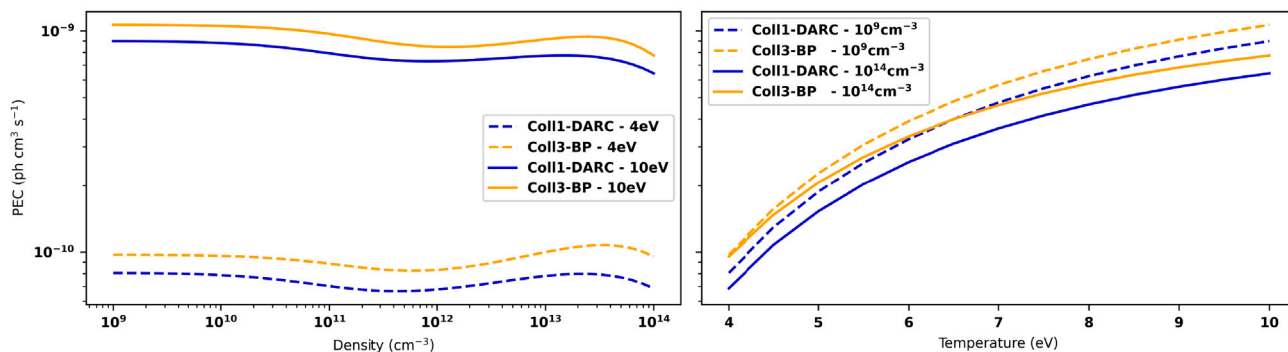
Fig. 8. Photon emissivity coefficient (PEC) as a function of density (left panel) and temperature (right panel) for the $3s^2 3p^4(^3P)4s\ ^2P_{3/2}$ - $3s^2 3p^4(^3P)4p\ ^2D^o_{5/2}$ $(11-37)$ transition. The blue and orange lines denote the Coll1-DARC and Coll3-BP calculations respectively, with dashed lines representing low densities and temperatures and the solid lines representing high densities and temperatures.

intermediate density region $10^{11} \leq n_e \leq 10^{14}$ cm^{-3}, there is a slight density dependence, although it remains significantly weaker than that of the temperature dependence which retains a positive gradient.

To search for relevant line ratios, a wavelength window between 407 nm and 490 nm was chosen and the strongest 50 lines within this region were considered. These line ratios were filtered with a maximum allowed value of 10 and cross-validated between the Coll1-DARC and Coll3-BP calculations, Coll2-ICFT was omitted in these comparisons due to NIST spectroscopic wavelengths not being adopted. A-values have a significant impact on the photon emissivity coefficients and a lack of shifted wavelengths when evaluating the A-values make the comparison less robust. Two exemplar line ratios are presented Figs. 9 and 10 for analysis.

Fig. 9 presents the line ratio of the 8–33 and 11–37 strong dipole transitions. We previously investigated both these lines for their sensitivities in Figs. 7 and 8 and denoted their suitability for potential use as temperature diagnostic. Both these transitions have their A-values recorded in Table 5 and the line ratio between the two calculations shows good agreement across the density spectrum, but particularly so in the low-density regime. There is also excellent agreement between the two calculations at 10 eV and 2 eV for both low and high density regimes. Fig. 10 presents the ratio for the 8–30 and 11–37 strong dipole transitions, a line denoted as diagnostically important in the work of Fantz et al. [2]. This is due to the lack of temperature dependence for this line ratio in the region of interest for fusion, $5 \times 10^{10} \leq n_e \leq 5 \times 10^{12}$ cm^{-3}. In Fig. 10 the x-axis is limited to between $2 \times 10^{11} \leq$

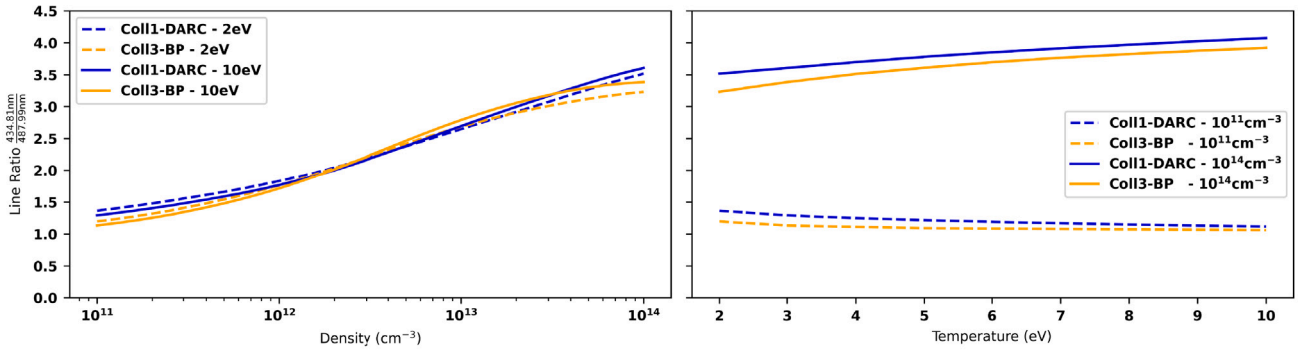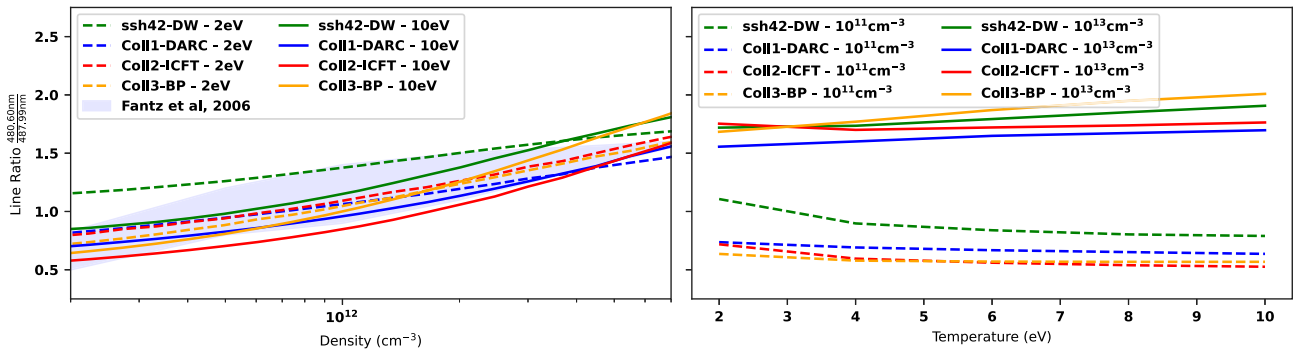**Fig. 9.** $\frac{8-33}{11-37}$ line ratio as a function of density (left panel) and temperature (right panel). The blue and orange lines denote the Coll1-DARC and Coll3-BP calculations, respectively, with dashed lines representing low densities and temperatures and the solid lines representing high densities and temperatures.

Fig. 10. $\frac{8-30}{11-37}$ line ratio as a function of density (left panel) and temperature (right panel). The blue and orange lines denote the Coll1-DARC and Coll3-BP calculations, whilst the red and green lines denote Coll2-ICFT and ssh42-DW calculations respectively, with dashed lines representing low densities and temperatures and the solid lines representing high densities and temperatures. The ssh42-DW calculation line ratios are recovered from Summers [23] for the $ssh42\_cs\_ic\#ar1.dat$ adf04 file of Stuart Henderson at UKAEA. This figure was prepared using results from ADAS208. Summers [23].

$n_e \leq 7 \times 10^{12}$ cm^{-3} in line with the data available from Fantz et al. [2]. All three collisional calculations exhibit significant agreement when compared to each other indicating a good density diagnostic.

4.3. Experimental benchmark

The Compact Toroidal Hybrid (CTH) at Auburn University is a low-aspect-ratio ($A \geq 3.5$) torsatron with a major radius of $R_0 = 0.75$ m [62]. A series of vertical, toroidal, and helical magnetic field coils provide a stellarator magnetic configuration used for this work in conjunction with electron cyclotron resonance heating (ECRH) that allows access to electron temperatures between 1 and 10 eV. A triple tipped Langmuir probe inserted into the plasma is used to measure the electron temperature and density. Plasmas on CTH last approximately 100 ms. A Princeton Instruments HRS-500 spectrometer used in conjunction with a PIXIS camera obtains spectra with an exposure time of approximately 10 ms. Both electron temperature and density are relatively constant over the observed plasma path length and for the duration of a single exposure.

A single, representative spectrum is shown in Fig. 11 for which the electron temperature is 7 eV and the electron density is 2.1×10^{11} cm^{-3}. The top graph shows the experimental spectrum in purple. In orange and green are shown the output of the time-dependent Collisional Radiative Model solver using the rates described here, at a time of 1.1×10^{-3} ms and electron density and temperatures. The BP calculation is shown in orange and the DARC calculation is shown in green. Both are normalized to the 460.96 nm wavelength line. The bottom graph shows the % difference between the synthetic and experimental intensities to better observe the quality of fit for the smaller wavelengths. Lines are excluded for comparison which have an Einstein A coefficient uncertainty from NIST above 10%, as well as blending with other lines.
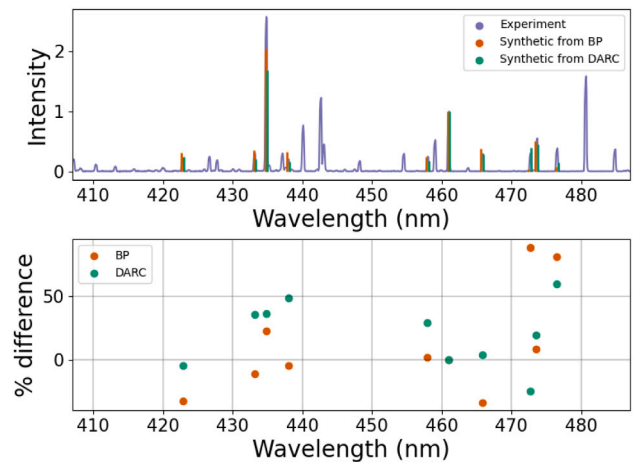

Fig. 11. Comparison between synthetic and experimental data on CTH. The synthetic model uses a time-dependent Collisional Radiative Model with a time of 1.1×10^{-3} ms, along with the electron temperature and density values measured by the triple-tipped Langmuir probe inserted into the plasma. Percentage errors indicate difference between peak values in synthetic and experimental spectra within the selected normalized scheme, defined as 100×(Experimental-Synthetic)/Experimental.

Excellent agreement is found for some lines with the synthetic model correctly predicting the strongest lines observed. The differences in the spectral heights is being investigated as part of future work, with differences most likely due to non-steady state conditions in the Ar ɪɪ ground and metastable populations.

5. Conclusions

In this paper we have investigated three separate, independent atomic structure calculations for Ar II. The calculated energy levels and A-values have been compared and contrasted between the three structures and the experimental values recorded in the NIST database. The structure models were then used for computing electron-impact excitation cross sections using three different R-matrix methodologies, PDARC, ICFT and BP with pesudostates which adopt three independent collisional codes. Each model was shown to produce similar resonance structures in the collision strengths for a selection of forbidden, weak and strong dipole transitions. The corresponding Maxwellian averaged effective collision strengths were also computed and found to show a high degree of agreement between the three calculations.

The fractional populations of the excited states of Ar II, at a given temperature and density, were modelled and compared for the three calculations. The observations made showed excellent agreement for all spectroscopic levels. The total power loss for all three calculations was also computed and a significant agreement was found between the calculations when considering only $n = 4$ states which lie below the ionization potential. Deviations became evident when the $n = 5$ levels were included in the computations but it was shown that the addition of the $n = 6$ levels made little to no contribution. Hence we conclude that the PLT curve has converged when all levels up to $n = 5$ are incorporated in the modelling.

Possible diagnostic lines and line ratios were systematically searched for and identified and, where possible, compared with experimental spectra taken from the Compact Toroidal Hybrid (CTH). Additionally, the diagnostically important for fusion 480 nm/488 nm line ratio was investigated and compared with previous theoretical calculations available in the OPEN-ADAS database. Excellent agreement was found for this line ratio indicating convergence between the calculations.

The recommended data file for use in modelling applications is the one computed using Model 3 for the structure calculation and Coll3-BP for the electron-impact excitation computations. The reasons for this choice are threefold. Firstly, the energies of the target states included have been shifted to their experimental positions which will help in any line identifications. Secondly, the transition probabilities (A-values) and excitation rates have been generated using these shifted energies to improve accuracy. Finally, the line radiation power loss coefficient (PLT) computed using this data set includes the $n = 5$ levels below the ionization potential and is in excellent agreement with the ICFT calculation. All of these conclusions give confidence in the convergence of this work.

CRediT authorship contribution statement

N.E. McElroy: Writing – review & editing, Writing – original draft, Visualization, Validation, Methodology, Investigation, Formal analysis. **C.A. Ramsbottom:** Writing – review & editing, Writing – original draft, Validation, Supervision, Methodology, Investigation. **C.P. Ballance:** Writing – review & editing, Writing – original draft, Validation, Supervision. **N.R. Badnell:** Writing – review & editing, Methodology, Investigation. **M.G. O'Mullane:** Writing – review & editing, Validation, Conceptualization. **S.D. Loch:** Writing – review & editing, Validation, Supervision. **E.N. Williamson:** Writing – review & editing, Writing – original draft, Visualization, Data curation.

Declaration of competing interest

The authors declare that they have no known competing financial interests or personal relationships that could have appeared to influence the work reported in this paper.

Data availability

Data will be made available on request.

References

[1] Hamdi R, Nessib NB, Bréchot SS, Dimitrijević M. Atoms 2017;5(4):26. http://dx.doi.org/10.3390/atoms5030026.

[2] Fantz U, Falter H, Franzen P, Wünderlich D, Berger M, Lorenz A, Kraus W, McNeely P, Riedl R, Speth E. Nucl Fusion 2006;46(6):S297–306. http://dx.doi.org/10.1088/0029-5515/46/6/s10.

[3] Jachmich S, Kruezi U, Lehnen M, Baruzzo M, Baylor L, Carnevale D, Craven D, Eidietis N, Ficker O, Gebhart T, Gerasimov S, Herfindal J, Hollmann E, Huber A, Lomas P, Lovell J, Manzanares A, Maslov M, Mlynar J, Pautasso G, Paz-Soldan C, Peacock A, Piron L, Plyusnin V, Reinke M, Reux C, Rimini F, Sheikh U, Shiraki D, Silburn S, Sweeney R, Wilson J, Carvalho P, the JET Contributors. Nucl Fusion 2021;62(2):026012. http://dx.doi.org/10.1088/1741-4326/ac3c86.

[4] Li Y, Chen Z, Yan W, Wei Y, Tong R, Lin Z, Li W, Bai W, Wang N, Li D, Chen Z, Jiang Z, Yang Z, Ding Y, Pan Y, the J-TEXT Team. Nucl Fusion 2021;61(12):126025. http://dx.doi.org/10.1088/1741-4326/ac2cf7.

[5] Reux C, Paz-Soldan C, Eidietis N, Lehnen M, Aleynikov P, Silburn S, Bandaru V, Ficker O, Hoelzl M, Hollmann EM, Jachmich S, Joffrin E, Lomas PJ, Rimini F, Baylor L, Bleasdale A, Calacci L, Causa F, Carnevale D, Coffey I, Craven D, Molin AD, de la Luna E, Tommasi GD, Garcia J, Gebhart T, Giacomelli L, Huber A, Khilkevich E, Lowry C, Macusova E, Manzanares A, Nocente M, Panontin E, Papp G, Pautasso G, Peacock A, Plyusnin V, Shevelev A, Shiraki D, Sommariva C, Sozzi C, Sridhar S, Sweeney R, Szepesi G, Tinguely RA, Wilson J. Plasma Phys Control Fusion 2022;64(3):034002. http://dx.doi.org/10.1088/1361-6587/ac48bc.

[6] Keenan FP, Bates B, Dufton P, Holmgren DE, Gilheany S. Astrophys J 1990;348:322–7.

[7] Holmgren DE, Brown PJF, Dufton P, Keenan FP. Astrophys J 1990;364:657–62.

[8] Wessmayer D, Przybilla N, Butler K. Astron Astrophys 2022.

[9] Heber U, Edelmann H. Astrophys Space Sci 2004;291(3):341–9. http://dx.doi.org/10.1023/b:astr.0000044342.79287.fc.

[10] Kupfer T, Przybilla N, Heber U, Jeffery CS, Behara N, Butler K, California Institute of Technology, Universitat Innsbruck, University of Erlangen-Nuremberg, Armagh Observatory, Planetarium, University Observatory Munich. Mon Not R Astron Soc 2017;471:877–90.

[11] Kwok LA, Siebert MR, Johansson J, Jha SW, Blondin S, Dessart L, Foley RJ, Hillier DJ, Larison C, Pakmor R, Temim T, Andrews JE, Auchettl K, Badenes C, Barna B, Bostroem KA, Newman MJB, Brink TG, Bustamante-Rosell MJ, Camacho-Neves Y, Clocchiatti A, Coulter DA, Davis KW, Deckers M, Dimitriadis G, Dong Y, Farah JR, Filippenko AV, Flors A, Fox OD, Garnavich PM, Gonzalez EP, Graur O, Hambsch F-J, Hosseinzadeh G, Howell DA, Hughes JP, Kerzendorf WE, Saux XKL, Maeda K, Maguire K, McCully C, Mihalenko C, Newsome M, O'Brien JT, Pearson J, Pellegrino C, Pierel JDR, Polin A, Rest A, Rojas-Bravo C, Sand DJ, Schwab M, Shahbandeh M, Shrestha M, Smith N, Strolger LG, Szalai T, Taggart K, Terreran G, Terwel JH, Tinyanont S, Valenti S, Vinkó J, Wheeler JC, Yang Y, Zheng W, Ashall C, DerKacy JM, Galbany L, Hoeflich P, de Jaeger T, Lu J, Maund JR, Medler K, Morrell NI, Shappee BJ, Stritzinger MD, Suntzeff NB, Tucker MA, Wang L. Ground-based and JWST observations of SN 2022pul: II. Evidence from nebular spectroscopy for a violent merger in a peculiar type-ia supernova. 2023, URL https://api.semanticscholar.org/CorpusID:261101244.

[12] Pagomenos G. Gas and dust in galactic planetary nebulae at sub-solar metallicity (Ph.D. thesis), The Open University; 2017.

[13] Mendoza C, Bautista MA, Deprince J, García JA, Gatuzz E, Gorczyca TW, Kallman TR, Palmeri P, Quinet P, Witthoeft MC. Atoms 2021;9(1):12. http://dx.doi.org/10.3390/atoms9010012.

[14] Pal AF, Ryabinkin AN, Serov AO, Lopaev DV, Mankelevich YA, Rakhimov AT, Rakhimova TV, Baklanov MR. J Phys D: Appl Phys 2020;53(29):295202. http://dx.doi.org/10.1088/1361-6463/ab813f.

[15] Espinho S, Felizardo E, Henriques J, Tatarova E. J Appl Phys 2017;121(15):153303. http://dx.doi.org/10.1063/1.4981535.

[16] Thornton AJ, Gibson KJ, Harrison JR, Lehnen M, Martin R, and AK. Plasma Phys Control Fusion 2012;54(12):125007. http://dx.doi.org/10.1088/0741-3335/54/12/125007.

[17] Landman I, Pestchanyi S, Igitkhanov Y, Pitts R. J Nucl Mater 2013;438:S871–4. http://dx.doi.org/10.1016/j.jnucmat.2013.01.188.

[18] Hollmann EM, Bykov I, Eidietis NW, Herfindal JL, Lvovskiy A, Moyer RA, Parks PB, Paz-Soldan C, Pigarov AY, Rudakov DL, Shiraki D, Watkins J. Phys Plasmas 2020;27(4). http://dx.doi.org/10.1063/5.0003299.

[19] Jia G, Liu X, Xu G, Wang L, Zhu S, Xie H, Si H, Sang C, Yang Z, Xu J, Li H. Phys Plasmas 2020;27(6). http://dx.doi.org/10.1063/1.5133832.

[20] Ma H, Cao C, Cai L, Gao J, Du H, Wang D, Wu N, Liu L, Yang Z. Phys Scr 2023;98(11):115608. http://dx.doi.org/10.1088/1402-4896/acff49.

[21] Shimomura Y, Aymar R, Chuyanov V, Huguet M, Parker R, Team IJC. Nucl Fusion 1999;39(9Y):1295–308. http://dx.doi.org/10.1088/0029-5515/39/9y/307.

[22] Federici G, Bachmann C, Barucca L, Baylard C, Biel W, Boccaccini L, Bustreo C, Ciattaglia S, Cismondi F, Corato V, Day C, Diegele E, Franke T, Gaio E, Gliss C, Haertl T, Ibarra A, Holden J, Keech G, Kembleton R, Loving A, Maviglia F, Morris J, Meszaros B, Moscato I, Pintsuk G, Siccinio M, Taylor N, Tran M, Vorpahl C, Walden H, You J. Nucl Fusion 2019;59(6):066013. http://dx.doi.org/10.1088/1741-4326/ab1178.

[23] Summers HP. The ADAS user manual. 2004, http://www.adas.ac.uk.

[24] Dere KP, Landi E, Mason HE, Fossi BCM, Young PR. Astron Astrophys Suppl Ser 1997;125(1):149–73. http://dx.doi.org/10.1051/aas:1997368.

[25] Del Zanna G, Dere KP, Young PR, Landi E. Astrophys J 2021;909(1):38. http://dx.doi.org/10.3847/1538-4357/abd8ce.

[26] Hibbert A. Atoms 2017;5:8. http://dx.doi.org/10.3390/atoms5010008.

[27] Afaneh F, Hamasha S, Khateeb KA. Adv Stud Theor Phys 2016;10:235–66. http://dx.doi.org/10.12988/astp.2016.6314.

[28] Dipti, Srivastava R. J Quant Spectrosc Radiat Transfer 2016;176:12–23.

[29] Kwon DH, Cho Y-S. At Data Nucl Data Tables 2021;137:101385.

[30] Griffin DC, Ballance CP, Loch SD, Pindzola MS. J Phys B: At Mol Opt Phys 2007;40:4537–50.

[31] Pelan J, Berrington KA. Astron Astrophys 1995;110:209.

[32] Dyall K, Grant I, Johnson C, Parpia F, Plummer E. Comput Phys Comm 1989;55(3):425–56. http://dx.doi.org/10.1016/0010-4655(89)90136-7.

[33] Grant I, McKenzie B, Norrington P, Mayers D, Pyper N. Comput Phys Comm 1980;21(2):207–31. http://dx.doi.org/10.1016/0010-4655(80)90041-7.

[34] McKenzie B, Grant I, Norrington P. Comput Phys Comm 1980;21(2):233–46. http://dx.doi.org/10.1016/0010-4655(80)90042-9.

[35] Eissner W. Le J Phys IV 1991;01(C1):C1–3–C1–13. http://dx.doi.org/10.1051/jp4:1991101.

[36] Badnell NR. J Phys B: At Mol Phys 1986;19(22):3827–35. http://dx.doi.org/10.1088/0022-3700/19/22/023.

[37] Badnell NR. J Phys B: At Mol Opt Phys 1997;30(1):1–11. http://dx.doi.org/10.1088/0953-4075/30/1/005.

[38] Kramida A, Ralchenko Y, Reader J, NIST ASD Team. Nist atomic spectra database (ver. 5.10). 2022, [Online]. Available: https://physics.nist.gov/asd [2023, May 4].

[39] Saloman EB. J Phys Chem Ref Data 2010;39(3). http://dx.doi.org/10.1063/1.3337661.

[40] Badnell NR, Gorczyca TW. J Phys B At Mol Opt Phys 1997;30(8):2011–9.

[41] Gorczyca TW, Badnell NR. J Phys B At Mol Opt Phys 1997;30(17):3897–911.

[42] Statz H, Horrigan FA, Koozekanani SH, Tang CL, Koster GF. J Appl Phys 1965;36:2278–86. http://dx.doi.org/10.1063/1.1714463.

[43] Minnhagen L. J Opt Soc Am 1971;61(9):1257. http://dx.doi.org/10.1364/josa.61.001257.

[44] Bennett WR, Kindlmann PJ, Mercer GN. Appl Opt 1965;4(S1):34. http://dx.doi.org/10.1364/ao.4.s1.000034.

[45] Whaling W, Anderson W, Carle M, Brault J, Zarem H. J Quant Spectrosc Radiat Transfer 1995;53(1):1–22. http://dx.doi.org/10.1016/0022-4073(94)00102-d.

[46] Minnhagen L. Ark Fys (Stockholm) 1959;14(31):483–95.

[47] Lawrence GM. 1967.

[48] Burke PG. R-matrix theory of atomic collisions. Springer Berlin Heidelberg; 2011, http://dx.doi.org/10.1007/978-3-642-15931-2.

[49] Burgess A, Sheorey VB. J Phys B: At Mol Phys 1974;7(17):2403–16. http://dx.doi.org/10.1088/0022-3700/7/17/026.

[50] Burke VM, Seaton MJ. J Phys B: At Mol Phys 1986;19(15):L527–33. http://dx.doi.org/10.1088/0022-3700/19/15/002.

[51] Burgess A, Tully JA. Astron Astrophys 1992;254:436–53.

[52] Ballance CP. Parallel R-matrix codes. 2023, http://connorb.freeshell.org/.

[53] Norrington PH. DARC. 2004, [DEFUNCT]http://www.am.qub.ac.uk/DARC.

[54] Norrington PH, Grant IP. J Phys B: At Mol Phys 1987;20(18):4869–81. http://dx.doi.org/10.1088/0022-3700/20/18/023.

[55] Hummer DG, Berrington KA, Eissner W, Pradhan AK, Saraph HE, Tully JA. Astron Astrophys 1993;279:298–309.

[56] Berrington KA, Eissner WB, Norrington PH. Comput Phys Comm 1995;92(2–3):290–420. http://dx.doi.org/10.1016/0010-4655(95)00123-8.

[57] Berrington KA, Burke PG, Butler K, Seaton MJ, Storey PJ, Taylor KT, Yan Y. J Phys B: At Mol Phys 1987;20(23):6379–97. http://dx.doi.org/10.1088/0022-3700/20/23/027.

[58] Badnell NR. J Phys B: At Mol Opt Phys 1999;32(23):5583–91. http://dx.doi.org/10.1088/0953-4075/32/23/312.

[59] Griffin DC, Badnell NR, Pindzola MS. J Phys B: At Mol Opt Phys 1998;31(16):3713–27. http://dx.doi.org/10.1088/0953-4075/31/16/022.

[60] Summers HP, Dickson WJ, O'Mullane MG, Badnell NR, Whiteford AD, Brooks DH, Lang J, Loch SD, Griffin DC. Plasma Phys Control Fusion 2006;48(2):263–93. http://dx.doi.org/10.1088/0741-3335/48/2/007.

[61] Johnson CA, Loch SD, Ennis DA. Nucl Mater Energy 2018;(2). http://dx.doi.org/10.1016/j.nme.2019.01.013.

[62] Hartwell G, Knowlton SF, Hanson JD, Ennis DA, Maurer DA. Fusion Sci Technol 2017.

[63] Griffin DC, Ballance CP, Pindzola MS, Robicheaux F, Loch SD, Ludlow JA, Witthoeft MC, Colgan J, Fontes CJ, Schultz DR. J Phys B: At Mol Opt Phys 2005;38(12):L199–206. http://dx.doi.org/10.1088/0953-4075/38/12/l01.